ACS MATERIALS Au
AN OPEN ACCESS JOURNAL OF THE AMERICAN CHEMICAL SOCIETY

pubs.acs.org/materialsau
Article

In Vivo Assessment of a Triple Periodic Minimal Surface Based Biomimmetic Gyroid as an Implant Material in a Rabbit Tibia Model

Pearlin Amaan Khan, Ansheed Raheem, Cheirmadurai Kalirajan, Konda Gokuldoss Prashanth, and Geetha Manivasagam*

Cite This: ACS Mater. Au 2024, 4, 479–488
Read Online
ACCESS | Metrics & More | Article Recommendations

ABSTRACT: Biomimetic approaches to implant construction are a rising frontier in implantology. Triple Periodic Minimal Surface (TPMS)-based additively manufactured gyroid structures offer a mean curvature of zero, rendering this structure an ideal porous architecture. Previous studies have demonstrated the ability of these structures to effectively mimic the mechanical cues required for optimal implant construction. The porous nature of gyroid materials enhances bone ingrowth, thereby improving implant stability within the body. This enhancement is attributed to the increased surface area of the gyroid structure, which is approximately 185% higher than that of a dense material of the same form factor. This larger surface area allows for enhanced cellular attachment and nutrient circulation facilitated by the porous channels. This study aims to evaluate the biological performance of a gyroid-based Ti6Al-4V implant material compared to a dense alloy counterpart. Cellular viability was assessed using the lactate dehydrogenase (LDH) assay, which demonstrated that the gyroid surface allowed marginally higher viability than dense material. The *in vivo* integration was studied over 6 weeks using a rabbit tibia model and characterized using X-ray, micro-CT, and histopathological examination. With a metal volume of 8.1%, the gyroid exhibited a bone volume/total volume (BV/TV) ratio of 9.6%, which is 11-fold higher than that of dense metal (0.8%). Histological assessments revealed neovascularization, in-bone growth, and the presence of a Haversian system in the gyroid structure, hinting at superior osteointegration.

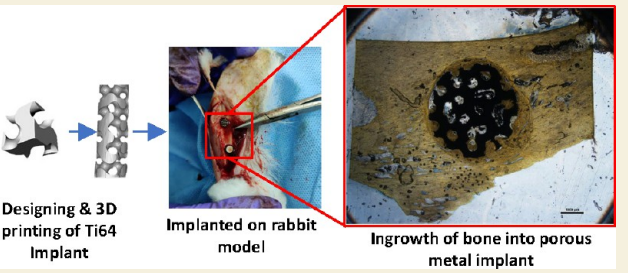

KEYWORDS: *Biomimetics, gyroid, Ti6Al4V, bone ingrowth, rabbit model, histopathology, micro-CT*

The orthopedic implant market stands as a burgeoning sector within the medical industry, poised for significant growth in the coming years. Projections indicate a notable compound annual growth rate (CAGR) of 6.2% through the years, reaching $56.5 billion market valuation by 2030.[1,2] Factors contributing to this growth include an increase in the aging population,[3] increased prevalence of musculoskeletal disorders,[4] lifestyle disorders such as obesity,[5] trauma-related orthopedic injuries,[6] improvements in manufacturing technology,[7] and changes in governmental and health insurance policies.[8,9] Metals are preferred materials in orthopedic implantology primarily owing to their superior capacity for bearing stress. Titanium, stainless steel, and cobalt chrome are the popular clinical choices, largely due to their demonstrated biocompatibility.[10] Among all available materials, titanium has emerged as the preferred choice for metal implants, primarily due to its high strength, low density, and superior corrosion resistance. Furthermore, titanium is a non-dielectric material, which does not interfere with Magnetic Resonance Imaging, solidifying its role as a crucial orthopedic implant material over the past few decades.[11,12] Studies have observed that titanium and its alloys elicit a particularly lower adverse immune response compared to other materials, such as stainless steel, which are known to exhibit increased expression of pro-inflammatory markers like MD2, TLR-4, and MyD88. Cobalt–chromium alloys have also been reported to cause osteolysis through inflammatory cytokines.[13] While metals like titanium demonstrate favorable biocompatibility by reducing the likelihood of inflammatory immune responses, they lack interaction with the human body, largely attributable to their bioinert properties.[14] The degree of bioinertness alone does not ensure the success of an implant; instead, a metric of "implant performance over the service period" is crucial for evaluating efficacy.[15]

Reports on improving implantology have highlighted two fundamental insights that have the potential to address the inherent impediments in the existing implantation strategy,

Received: February 29, 2024
Revised: May 19, 2024
Accepted: May 22, 2024
Published: June 13, 2024

thereby enhancing its success rate. Cell−material crosstalk[16] and mechanical homogeneity[17] are two important factors that could improve the bioactivity of implants. The interaction between various types of cells at the site of implantation and the implant material can influence the integration and stability of the implant within the body. The surface properties of the implant, such as its roughness, chemistry, surface energy, wettability, and charge, can affect how cells attach to and grow on the implant, as well as the release of any bioactive molecules.[18] The mechanical bulk properties of an implant, like its stiffness, elasticity, strength, fatigue resistance, wear, and corrosion resistance, intricately shape cellular responses.[19] While existing implant materials offer superior mechanical properties compared to human bone, this surplus leads to an unnatural stress distribution, resulting in phenomena like stress shielding.[20] This increased strength of metal implants causes them to bear a disproportionate share of the load, leading to improper load distribution when used in load-bearing applications such as trauma implants for fixing long bone defects or total hip arthroplasty, subsequently resulting in disuse osteopenia.[21,22] Many factors, including those above, dictate this intricate interplay between human cells and material surfaces, finally deciding the fate of an implant inside a human body. Deviation from the natural properties of bone can precipitate epigenetic alterations, ultimately instigating immune responses that may culminate in implant failure over time.[23]

One of the key engineering interventions to address the shortcomings in existing implantology is to adopt biomimetic strategies for implant construction, thereby facilitating bioactive interactions.[24] With the advent of advanced additive manufacturing technologies, material porosity can now be engineered and manufactured at the micrometer scale, a task that was previously daunting with conventional manufacturing processes.[25] These developments motivated our team to engage in biomimetic implant design by reducing material strength to match that of human bone through porosity engineering and fabricating it using additive manufacturing technology. In our previous study by Hameed et al. in 2021, a Triply Periodic Minimal Surface (TPMS) with zero mean curvature was designed, whose isometry eliminates stress concentrations.[24,26,27] Briefly, grade 23 Ti-6Al-4V powder was selected for its obvious benefits and used for 3D printing the porous structures with a gyroid architecture. The porous structure used in this study was designed, characterized, and tested under *in vitro* conditions. Four gyroid unit cells corresponding to four different pore sizes (250, 300, 350, and 400 μm) were created in Rhino 3D and populated into a cuboidal geometry using Materialize Magics. The structures were then 3D printed using Selective Laser Melting technology, followed by material characterization and *in vitro* biocompatibility analysis. This study revealed that a pore size of 250 μm exhibited superior compressive strength of 205.7 MPa, with analogous biocompatibility to other pore sizes (300, 350, and 400 μm) and thus was chosen for further evaluation. The surface was rendered porous to enhance the available surface area for cellular interaction, thereby offering multiple advantages. One advantage is that the porous implant body offers a larger surface area for cellular attachment, along with the establishment of a microenvironment that closely mimics the extracellular matrix (ECM) of the body. These conditions facilitated enhanced cellular adhesion, spreading, and differentiation on the surface.[24] Also, porous surfaces can also allow for the infiltration of nutrients, gases, and other molecules that are important for cell survival and function.[28] Porous surfaces can be used to create a gradient in the elastic modulus of an implant, with the pores having a lower elastic modulus than the surrounding material, thus reducing the overall elastic modulus to match that of natural human bone, thereby reducing the stress shielding effect.[29]

While mechanical and *in vitro* performance was satisfactory in the previous study, it is imperative to ascertain the real-world performance of the structure in an animal model as a first step toward clinical translation. In general, similar bone-mimicking implant design research studies often conclude with *in vitro* analysis, which may not fully replicate the complex interactions between devices/materials and living systems.[30] Given that the design differs morphologically from currently available implants, conducting *in vivo* testing is a critical step in assessing the efficacy of the new design and meeting various regulatory requirements toward societal advancement.[31] Thus, this study aims to assess the *in vivo* performance of the 250 μm gyroid architecture in a rabbit tibia model.[24] Rabbits offer advantages in terms of availability, ease of handling, cost-effectiveness, and ethical compliance in animal testing protocols.[32] Researchers have observed similarities in the mid-diaphyseal bone region between rabbits and humans with respect to fracture toughness and bone mineral density.[33] Additionally, compared to other small animals, rabbit skeletal development and bone turnover are faster; therefore, the rabbit model was selected for this study.[34,27] Since the tibial girth is smaller than the femoral girth, and the tibia in rabbits is easier to access than the femur, researchers have opted for small-sized defects and implants less than or equal to 5 mm in diameter in the tibial region.

This study compares a commercial dense implant material, Ti-6AL-4V (ASTM grade 5/UNS R56400), with the 3D printed porous gyroid material of the same composition in both *in vitro* and *in vivo* aspects. Through comparative analysis with the dense material, factors such as bone ingrowth and the osteogenic potential of the porous structure can be identified. This investigation further elucidates the dynamic interplay between porosity and *de novo* bone tissue−material interactions, shedding light on the active role of porosity in facilitating tissue infiltration and fostering crosstalk.

EXPERIMENTAL METHODS

Design and Manufacturing of Scaffolds

Gyroid implants with pore sizes of 250 μm were selected for this study based on the results obtained from the previous report.[24] The implants were designed and fabricated as described in our earlier work.[24] Briefly, Rhino6.0 and the grasshopper plug-in were used to model the individual unit cells of the gyroid. Using the "structure" tool in Materialize Magics 20.03, the STL model of gyroid implants was populated into a cylindrical shape with a 3.5 mm diameter and 40 mm length, as illustrated in Figure 1. The STL model is then 3D printed in a laser-based powder bed fusion metal 3D printer (SLM280, Germany) using grade 23 Ti-6Al-4V powder from Sandvik Osprey, United Kingdom. The fabricated rods were then cut into smaller sections with 4 mm height suitable for *in vivo* study. Similarly, dense implants with 3.5 mm × 4 mm height were produced using a SLM50 laser-based powder bed fusion device (Realizer GmbH-Germany). The surface area and volume of the dense titanium alloy and the 3D-printed porous structures were measured computationally in Materialize Magics.

https://doi.org/10.1021/acsmaterialsau.4c00016
ACS Mater. Au 2024, 4, 479−488

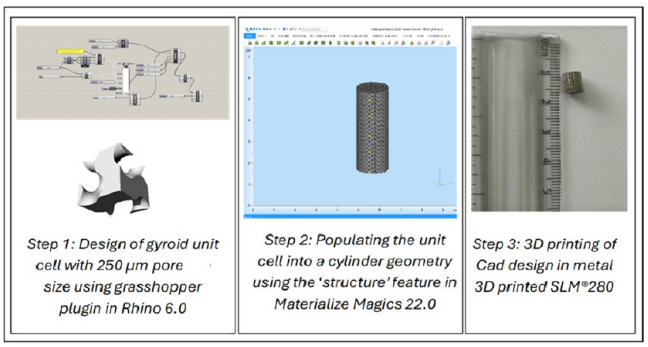

Figure 1. Schematics of gyroid implant design.

Postprocessing: Acid Etching

The printed samples were etched in Kroll's reagent, which consisted of a HF/HNO_3 solution to remove any loosely bound and unmelted powder. Using an ultrasonic cleaner, the powders trapped within the porous gyroid structure were first removed by compressed air and multiple washings in distilled water. The samples were then immersed in Kroll's reagent for 5 min, followed by washing with distilled water five times.[35] Conversely, the dense samples were not etched but polished with grid papers to achieve a mirror finish. A scanning electron microscope (SEM) (Zeiss EVO MA 15, Germany) was used to observe the microscopic features of the gyroid samples before and after chemical polishing. Both samples were then autoclaved and used for *in vitro* and *in vivo* studies.

Cytotoxicity Assay: *In Vitro* Study

For biocompatibility studies, 3D printed porous Gyroid samples cut in disc shape with 10 mm diameter and 1 mm height were used. Human mesenchymal stem cells (hMSCs) were procured and cultured as described in the previous study.[36] Briefly, hMSCs were expanded in Alpha-modified Eagle medium (Alpha MEM, Gibco), along with 10% fetal bovine serum (FBS, Hi-Media) and 1% Penstrep (Himedia), at 37 °C in a humidified atmosphere containing 5% CO_2. For the cell proliferation assay and fluorescence imaging, hMSCs between passages 3 and 5 were used. Samples were cleaned with 70% alcohol, followed by autoclaving for sterilization. The cell seeding density for the experiment was 1×10^4 cells/cm^2 and 2×10^4 cells/cm^2. For cytotoxicity assay, after 48 h of incubation, LDH Reagent from CyQUANT LDH Cytotoxicity Assay (Thermofisher) was used according to manufacturer protocol. The calorimetric readings were obtained using a microplate absorbance reader (Biorad) at 490 and 680 nm.

Fluorescence Imaging: *In Vitro* Study

Before seeding hMSCs, the flask containing cells was stained with Dil dye 2.5 mg/mL (D391,1 Thermofisher) for 5 min as per manufacturer protocol. This was followed by trypsinization and seeding on the samples of gyroid and dense titanium alloy, and after 24 h of incubation, the cells were fixed with 4% paraformaldehyde. Using Triton X 0.01%, cells were permeabilized and washed with PBS thrice, followed by incubation with FITC phalloidin (P5282, Merck) for 40 min to visualize actin cytoskeleton. The nucleus was stained 10 min before imaging by adding DAPI stain (D9542, Merck) at 300 ng/mL concentration, and the lipophilic structures were stained using Dil stain (D3911, Invitrogen) at 2 μM concentration. The samples were observed in Evos M500, a fluorescence microscope.

X-ray Scanning and Micro-CT Analysis

The rabbit tibias implanted with 3D implants were scanned using micro-CT (BioSpec 70/30USR, Bruker) to determine the osteointegration and infiltration of new bone growth. The scanning parameters were set as follows: X-ray source voltage = 90 kV; beam current = 200 μA; scanning resolution = 20 μm. After scanning the sample, the projection is reconstructed and segmented into a binary image and further analyzed with Microview by Parallax Innovation Inc. The internal space of the scaffold and bone tissue growth into the scaffold was defined as the region of interest, and the bone volume (BV), metal volume (MV), and total pore volume (TV) were measured by micro-CT for further detailed data analysis. Briefly, the scanned files were uploaded, and a cylindrical region of interest was defined, which was fixed for all samples. The threshold was adjusted to only detect bone or metal. Further, bone mineral density (BMD) was measured using a bone analysis tool. By calculating the ratio of BV to TV (BV/TV) and MV to TV (MV/TV), the bone growth and metal volume were quantitatively evaluated.

Surgical Procedure

Twelve male New Zealand white rabbits, after sanctioning by Vellore Institute of Technology (VIT)'s Institutional Animal Ethical Committee (IAEC) (VIT/IAEC/18/Dec2020/04), weighing about 1.8−2.2 kg were caged in VIT animal house with standard chow and water and frequent leafy vegetables. Before starting the surgery, the thickness of the bone was assessed using CT in the smallest rabbit of the group to confirm that the diameter of the rabbit tibia would accommodate the implants, as illustrated in Figure 2a. Two implants 1

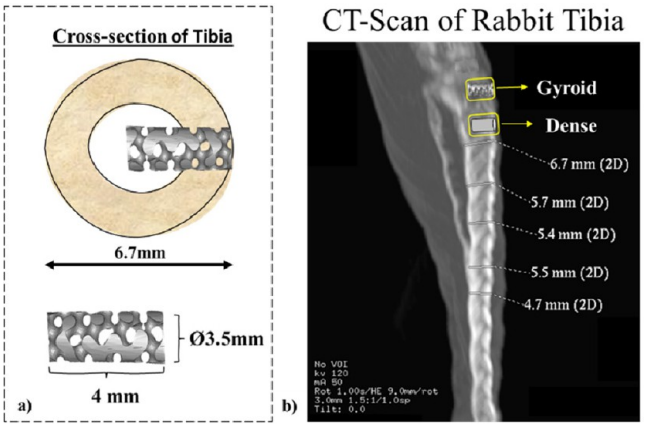

Figure 2. Bone width analysis. (a) Visualization of the cross-sectional profile of the rabbit tibia featuring the gyroid implant, including implant dimensions. (b) Computed Tomography (CT) imaging of the rabbit tibia was utilized for the evaluation of bone diameter.

cm apart, as shown in Figure 2b, were placed in each rabbit's right tibia as per ISO 10993-6:2016. Animals were anesthetized using ketamine and xylazine (60 mg/kg and 10 mg/kg, respectively). The surgical site, the medial aspect of the left tibia, was properly shaved and smeared with PV/I, as shown in Figure 3a, and the incision was placed using BP Handle and blade 22 as in Figure 3b. Local anesthesia, lignocaine (2% conc) was given as a local infiltration (QS). The medial aspect of the tibia was visualized as in Figure 3c,d, and the periosteum was elevated under saline irrigation; holes were made with a 702 surgical bur as shown in Figure 3e,f. After sanitization of the hole, sterile implants were placed, as shown in Figure 3g. Tissues were sutured with Ethicon nonabsorbable monofilament polyamide sutures as in Figure 3h. The site was given a spray dressing (Healex). Animals were given postoperative antibiotic gentamycin (10 mg/kg) SC and analgesics for 3 days, along with dexamethasone 0.1% im. Polyfluorochromes such as doxycycline (D9891, Sigma) dosage of 25 mg/kg in the 1st and 2nd week, Calcein Blue (M1255, Sigma) 30 mg/kg dose in the 3rd and 4th week, and Calcein Green (C0875, Sigma) 90 mg/kg dose in the 5th and 6th week were administered to stain the bone growth.

Histopathological Evaluation

The tibial specimens were fixed in 10% neutral buffer formalin, dehydrated in increasing ethanol concentration (70−100%), cleared using an acetone alcohol mixture, and embedded in methyl methacrylate (MMA). After polymerization in MMA, thick sections (70−100 μm) were cut from the PMMA block using a linear precision saw microtome (ACCUTOME 100, Struers, Denmark). The implant

https://doi.org/10.1021/acsmaterialsau.4c00016
ACS Mater. Au 2024, 4, 479−488

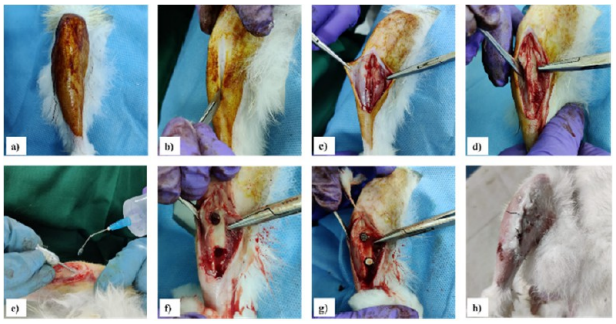

Figure 3. *In vivo* surgical procedure for implantation. (a) Administering surgical site disinfection with povidone iodine subsequent to hair removal. (b) Executing a 4 cm longitudinal incision. (c) Eliciting exposure of the medial aspect of the tibia by elevating the skin. (d) Facilitating exposure of the tibia through the manipulation of muscles with a periosteal elevator. (e) Conducting bone drilling with saline irrigation. (f) Creating two defect sites. (g) Implant placement. (h) Closure with sutures and application of Healex spray.

site was sectioned parallel to the long axis of the bone (i.e., cross-section of the implant with the surrounding cortical bone). These sections were stuck to the glass slide and ground, and the surface was polished using a variable speed grinder polisher (ECOMET 3000, Buehler, Germany). These sections were stained with hot Stevenel's blue and Van Gieson's picrofuchsin. This combination could highlight the pre-existing lamellar bone in light/dull yellow color, while the newly formed bone is typically bright yellowish in color. The osteoids are colored dark indigo blue, and the soft tissue surrounding them is stained light blue. The metal, being opaque, will be represented as dark black in color. Stained sections were evaluated in a trinocular transmitted light microscope (Nikon Ni Eclipse), and photomicrographs were captured using a camera (Nikon DS Ril) attached to the microscope.

Statistical Analysis

All graphical representations are displayed with error bars denoting the mean values along with the standard deviation (SD). Statistical comparisons were conducted utilizing the two-tailed Student's *t* test to determine significance. A threshold of $*p < 0.05$ was set to indicate statistical significance, while $**p < 0.001$ denoted highly significant differences.

RESULTS

Surface Volume and Morphology

The mechanical characterization of the gyroid was carried out in our previous work.[24] The gyroid and dense implant had a surface area of 248 mm^2 and 88 mm^2 as calculated computationally. Meanwhile, the approximate volume, as calculated computationally, was 29 mm^3 and 62 mm^3, respectively. The surface area and volume of the gyroid implant were calculated to be approximately 2.8 times more and 2.2 times less than the dense implant. The as-printed 3D gyroid structures exhibited much loose powder and unmelted powder attached to the structure, as shown in Figure 4b. The gyroid structures were cut into discs using wire cutting and etched chemically to remove loosely bound particles, as shown in Figure 4c. A similar strategy was also used by Wysocki et al. for manufacturing gyroid scaffolds using titanium metal powder.[35]

Cytotoxicity Assessment and Cytoskeletal Expansion

Ti-6Al-4V is a well-established biocompatible and bioinert material. Both dense and gyroid implants did not show any

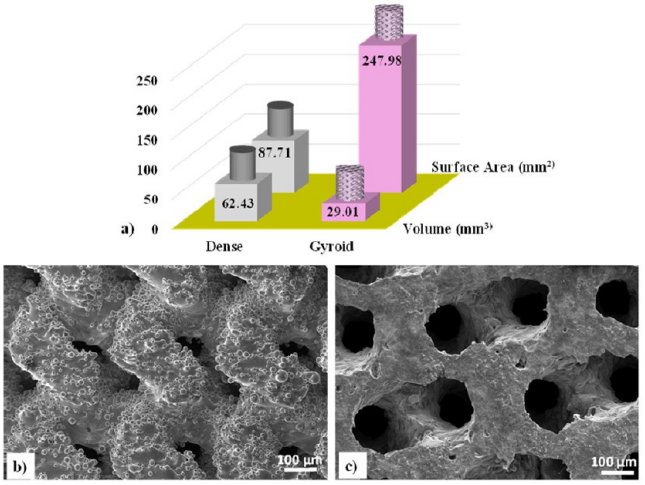

Figure 4. Morphological and volumetric analysis of samples. (a) Graphical depiction of the computationally derived surface area and volume metrics obtained using Materialise Magics software for both dense and gyroid structures. (b) SEM visualization illustrating the as printed gyroid structure, exhibiting remnants of unmelted powder at 40×. (c) SEM micrograph displaying the acid-etched sample, devoid of any residual unmelted powder particles at 40×.

cytotoxicity when compared to polystyrene control Figure 5a, thereby providing a healthy environment for stem cells to adhere. The fluorescence images shown in Figure 5b–k display healthy and well-spread hMSCs on the gyroid and dense surface. The blue fluorescence indicates the nucleus, the green color expresses the F-actin stress fibers, and the red fluorescence indicates the lipophilic stain. The cells display the characteristic widespread morphology of hMSCs, with round nuclei.

X-ray Scanning

After surgery to visualize the implants in live rabbits, X-rays were taken at intervals of 1st, 3rd, and 5th week. In the first week, in X-ray, as shown in Figure 6, the gyroid implant resembled a porous mesh structure while the dense implant was solid. X-ray images provide only gross information regarding implant stabilization and integration without any dislocation.

Micro-CT Analysis

The gyroid and dense implants were implanted at the distal end of the rabbit tibia, and the bone was harvested for micro-CT measurements after 6 weeks. The formation of bone inside the gyroid implant and around the dense implant was evaluated using Micro view. Figure 7c shows the 3D reconstruction image of the gyroid implant with new bone in yellow. As seen from the reconstructed images, the bone tissue in the gyroid scaffold infiltrated inside. At the end of 6 weeks, the ratio between BV and TV (BV/TV) was calculated by the quantitative analysis in Figure 7a. Within 6 weeks, the BV/TV ratios were approximately 9.6% for the gyroid implant and 0.8% for the dense implant. The bone formation in porous implants was almost ten times higher than in dense ones. As expected, in the dense implant, the metal volume was 17%, while in the gyroid one, it was almost half that at 8.1%, as shown in Figure 7b.

Sequential Polychrome Label Analysis

Three fluorescent labeling dyes were administered during the study. Doxycycline was used in the 1st and 2nd weeks, Calcein

https://doi.org/10.1021/acsmaterialsau.4c00016
ACS Mater. Au 2024, 4, 479–488

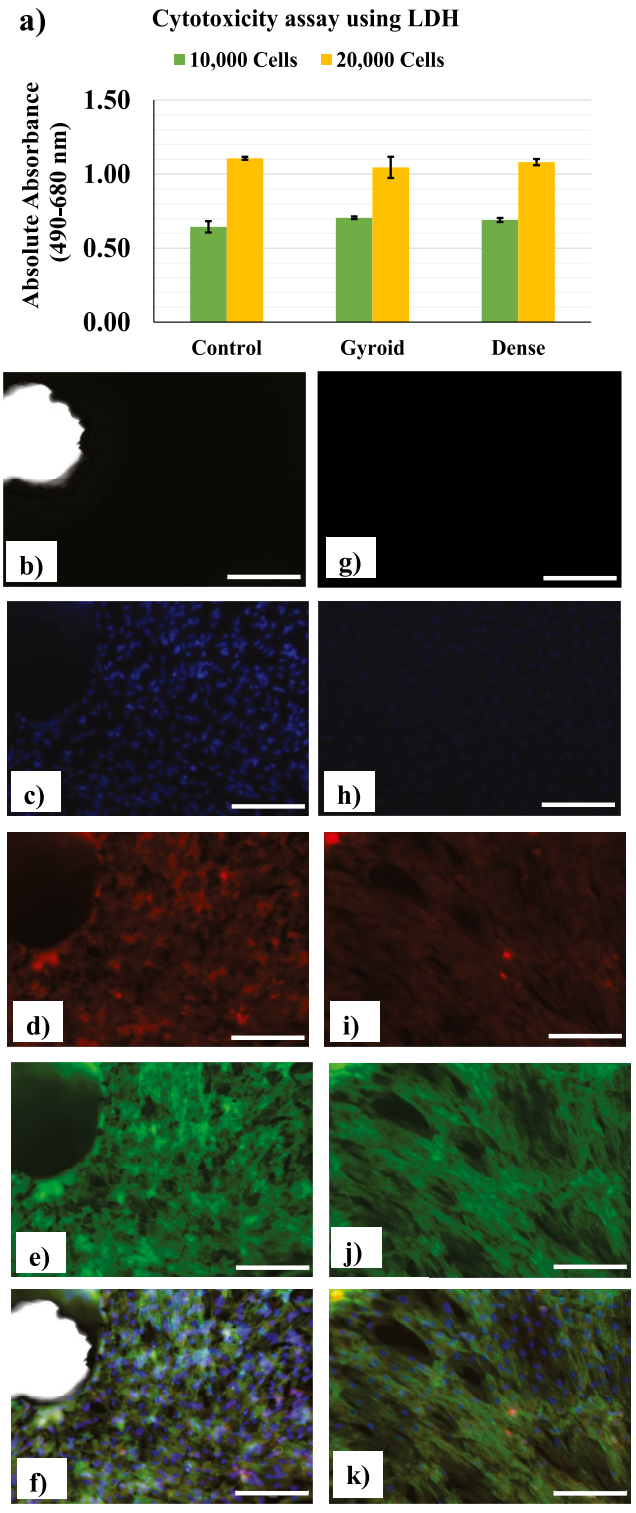

Figure 5. Cytotoxicity assessment and analysis of cytoskeletal expansion using fluorescent dye. (a) LDH assay-based cell viability assessment after 48 h of incubation using human mesenchymal stem cells (hMSCs). (b) Brightfield view of hMSCs adhered to the 3D-printed gyroid implant after 24 h of incubation. (c) Nuclear staining with DAPI of hMSCs on the 3D-printed gyroid implant after 24 h of incubation. (d) Lipophilic staining with DiI of hMSCs on the 3D-printed gyroid implant after 24 h of incubation. (e) Cytoskeleton staining (phalloidin) of hMSCs on the 3D-printed gyroid implant after 24 h of incubation. (f) Merged image of hMSCs on the 3D-printed gyroid implant after 24 h of incubation. (g) Brightfield view of hMSCs adhered to the dense implant after 24 h of incubation. (h) Nuclear staining with DAPI of hMSCs on the dense implant after 24 h of incubation. (i) Lipophilic staining with DiI of hMSCs on the dense implant after 24 h of incubation. (j) Cytoskeleton staining (phalloidin) of hMSCs on the dense implant after 24 h of incubation. (k) Merged image of hMSCs on the dense implant after 24 h of incubation. The scale bar represents 150 μm.

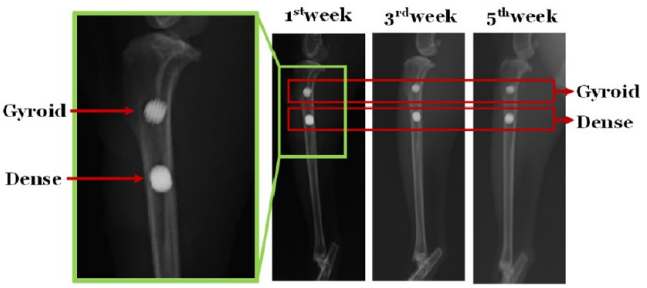

Figure 6. X-ray images of the rabbit tibia featuring both gyroid and dense implants, depicting implant status at the 1st, 3rd, and 5th week postsurgery intervals.

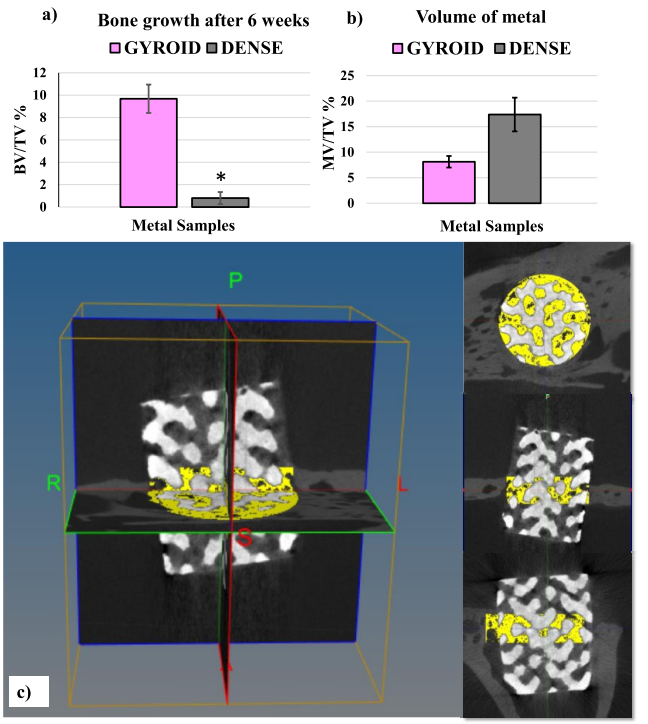

Figure 7. Micro-computed tomography reconstruction of the distal tibia of rabbits following a 6-week period of titanium gyroid and dense implantation. Quantitative analysis includes (a) bone volume fraction (BV/TV, %), (b) mineralized volume fraction (MV/TV, %), and (c) visualization of metal (white) and new bone (yellow). Statistical significance is denoted by $^*P < 0.05$.

Blue in the 3rd and 4th weeks, and Calcein Green in the 5th and 6th weeks. As seen in Figure 8a,d, new bone formation during the 1st and 2nd weeks showed a yellow color. The bone formed in the 3rd and 4th weeks emitted a strong blue color, as shown in Figure 8b,e, while the bone formed in the 5th and 6th weeks emitted a green color, as shown in Figure 8c,f. In the dense implant, new bone formation can be observed around the dense implant as no bone infiltrated the implant itself. In

https://doi.org/10.1021/acsmaterialsau.4c00016
ACS Mater. Au 2024, 4, 479−488

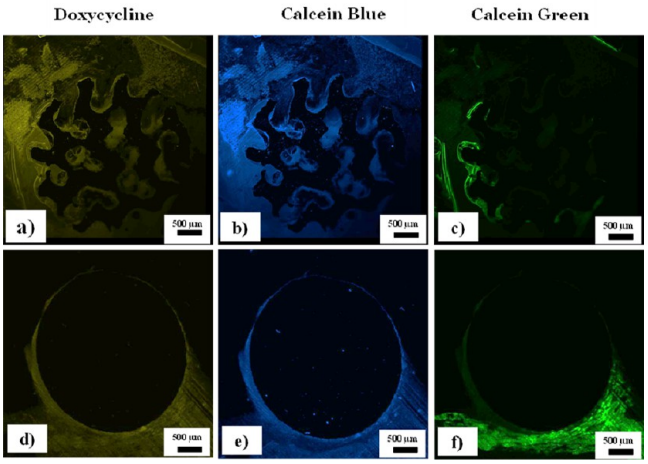

Figure 8. Sequential polychrome labeling. Over a 6-week duration in rabbit models, the following fluorescent dyes were administered: doxycycline (yellow) during weeks 1 and 2, Calcein Blue (blue) during weeks 3 and 4, and Calcein Green (green) during weeks 5 and 6. Labels a–c correspond to the gyroid group, while labels d–f pertain to the dense implant group.

contrast, in the gyroid implant, new bone infiltrated to the center from the very first 2 weeks onward.

Histology

As seen in Figure 9, bone tissue growth on the peripheral surface and inside the porous structure of the gyroid implant is

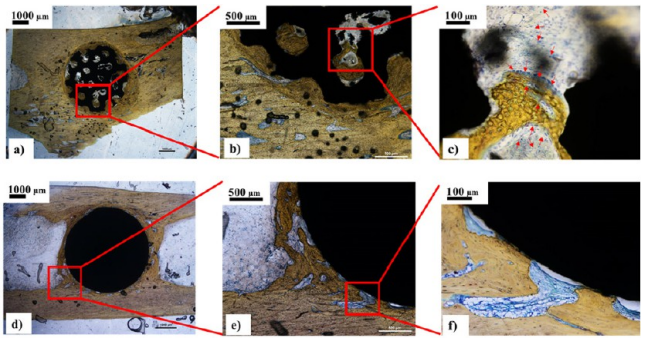

Figure 9. Histological analysis of tissues with implant harvested after 6 weeks. (a-c) Microphotographs of the histology section of the Gyroid implant with varying magnification. (d-f) Microphotographs of the histology section of the dense implant with varying magnification. Histology staining was performed with Stevenel's Blue and Van Gieson picrofuchsin counterstain postsacrifice after 6 weeks of bone healing. Black shadow represents the metal implant, dull yellow represents pre-existing bone, bright yellow represents new bone, light blue represents the soft tissues, and the red arrow points to the osteoid.

noted. No bone ingrowth can be witnessed in the dense samples, as shown in Figure 9d,f. Both samples exhibited soft tissue formation at the interface. The gyroid structure also demonstrated new bone infiltration within the pores of the implant, as shown in Figure 9c. A good apposition between the implant surface and new bone was present in both implants. However, due to the porous structure and irregular boundary, bone ingrowth at the periphery of the gyroid implant displayed better anchorage and bone tissue infiltration when compared to dense implants. As seen in Figure 9b, the new bone of the gyroid implant is covered by woven and lamellar-type bone tissue. Osteoblast cells line the new woven edge, and osteoid formation is evident at multiple regions, as shown in Figure 9c. Additionally, osteocytes (blue features) and Haversian system (dark shade) formation are noted in the new lamellar bone region, as seen in Figure 9c.

DISCUSSION

The investigation centered on the preclinical evaluation of a biomimetic Triple Periodic Minimal Surface (TPMS)-based gyroid architecture intended for the fabrication of load-bearing implants. Utilizing SLM additive manufacturing technology, the gyroid design was constructed using Ti-6Al-4V. Previous studies conducted within the laboratory found mechanical properties of the gyroid structure closely akin to those of natural bone.[37] Moreover, the preclinical analysis elaborated above demonstrated superior cellular material integration and bone ingrowth within the gyroid structure compared to dense alloy counterparts.

The gyroid pore sizes were determined based on a previous study by Hameed et al., where 250 μm was observed to yield adequate mechanical strength and biocompatibility.[24] Another study by Karageorgiou et al. corroborates this observation, according to which a pore size of 200 μm is necessary for the migration of osteoprogenitor cells and nutrient circulation into the pores of metal.[38] An increase of 185% in the total surface area available for cellular attachment could positively benefit the initial proliferation by providing additional binding sites for cells immediately after implantation, thus governing the stability of cell–material interaction. In general, materials with a larger surface area tend to have a greater number of available binding sites for cells, which can increase the strength and stability of the cell–material interaction. This can be beneficial in cases where it is desirable to promote cell adhesion, such as in the context of tissue engineering or the development of medical implants.[39] The gyroid had a surface area of 248 mm^2 while the dense material of the same dimension had only 88 mm^2, occupying a volume of 29 mm^3 as opposed to the 62 mm^3 of the dense material as illustrated in Figure 4a. There is a 3-fold increase in surface area with the same dimension, which positively contributes to improved cellular adhesion. The application of acid etching demonstrates a notable enhancement in mechanical properties within this study. This improvement is particularly significant as the presence of unmelted particles postadditive manufacturing may serve as potential initiators of failure. Addressing this concern is paramount, as these unmelted particles have been observed to potentially compromise tensile and fracture toughness properties.[40] Also, etching improved the surface finish of the sample, as shown in Figure 4c, which also contributes to optimal surface roughness, another parameter that influences cell viability.[41]

The cell viability, as illustrated in Figure 5a, was comparatively similar in both gyroid and dense samples, which is on par with the plastic control used in the study, where the latter had a marginal difference compared to the titanium samples. The assessment of viability at a seeding concentration of 10,000 cells reveals a slight superiority of metal samples over plastic controls, possibly attributed to the deviation from the optimal seeding concentration for the specific well plate. This discrepancy may be explained by the metal samples providing a more confined space for cellular interaction. However, at a seeding concentration of 20,000 cells, a more realistic depiction of cell viability emerges, where

https://doi.org/10.1021/acsmaterialsau.4c00016
ACS Mater. Au 2024, 4, 479–488

the optimal cell number ensures uniform viability across all cells.[42] In terms of relative viability, the gyroid structure exhibits higher viability compared to the dense alloy when referenced against the plastic control. This difference in viability may be attributed to the porous nature of the gyroid structure, which facilitates better integration with the surrounding environment, as elucidated by Li et al.[43]

Surface properties and topological features represent crucial elements, as discussed in the introduction, which exert significant influence over the immune response elicited by the implant.[44] Presented in Figure 5b−k are the cytoskeletal adjustments of the cells on the dense as well as on the gyroid structure revealed using fluorescent labeling. The analysis reveals similar cell density across both samples (gyroid and dense), yet distinct differences in cellular attachment patterns are evident. In the gyroid samples, cellular attachments appear more closely packed, with cells exhibiting an even spread. Conversely, cells on dense samples display elongated morphology, spreading unidirectionally. Notably, the gyroid structure induces a shift toward a rounded cytoskeletal arrangement, diverging from the typical spindle morphology observed in denser samples. This alteration in cell configuration is likely attributable to the comparatively higher surface roughness of the 3D-printed gyroid structure compared to the smoother surface of the dense material. The increased roughness is implicated in inducing morphological changes facilitated by the formation of peripheral focal adhesion complexes on rough surfaces, thereby prompting deviations in cellular morphology.[45,46]

The X-ray analysis shown in Figure 6 is a supplementary step in analyzing the implant placement postsurgery. The periodic assessment helps confirm implant alignment stability and identify tissue necrosis and bone integration.[47] Throughout the assessment period, both the gyroid and dense samples exhibited the expected performance without encountering any complications or inducing infections. Significantly, the gyroid sample exhibited remarkable bone ingrowth, as evidenced by the CT imaging analysis depicted in Figure 6. This observation underscores the superior performance of gyroid samples compared to dense counterparts, attributable to their higher surface area and interconnected porosity, facilitating enhanced bone integration.[48] The bone volume fraction of the gyroid (9.6%) was 12-fold higher than that of the dense sample (0.8%). This indicates that the porous sample had improved structural integrity. The metal volume was also lower for the gyroid at 8.1%, which is beneficial since it directly translates to a reduction in the modulus of elasticity compared to that of the dense. Similar porous structures have been studied in the past and have exhibited improved osteointegration and angiogenesis.[49]

Early stage bone ingrowth is important for successful osteointegration, a process notably observed in the gyroid sample as early as the 1st week, as demonstrated by fluorophore staining in Figure 8, indicative of doxycycline fluorescence. Subsequent bone formation during the 4th and 6th weeks further corroborates enhanced bone in-growth in the porous sample. Failure of correct initial bone formation may trigger a cascade of events, potentially leading to increased osteoclast generation and subsequent impairment of bone remodeling around the implant site.[50] Bone tissue growth both on the peripheral surface and inside the porous structure of the gyroid implant has been corroborated by the micro-CT data. The presence of pores within the gyroid structure enhances bone ingrowth and contributes to the mechanical interlocking between the implant and the surrounding bone tissue, leading to improved anchorage and stability.[51] This is exhibited as an 11-fold increase in BV/TV in gyroid samples compared to dense samples as shown in Figure 7a. Similarly, there is a significant 53% decrease in MV/TV in gyroids, meaning less metal is found in a specific volume while more bone occupies the same space as shown in Figure 7b. This could directly translate to a lower elastic modulus, bringing it closer to the range of natural human bone thus averting stress shielding which might explain why lattice structure-based implant design is burgeoning.[52] An exclusive find is the denovo bone formation in both gyroid sample exhibited in the histological data in Figure 9, with an improved vascularization noted within the pores of the gyroid structure. Neovascularization is essential for supplying nutrients and oxygen to the newly formed bone, which is vital for the proliferation of osteogenic cells. The gyroid structure exhibits de-novo bone groth and neovascularization within its pores, further supporting the idea that porous architectures can host a conducive environment for bone ingrowth and healing.[53] The presence of woven and lamellar bone types in the gyroid sample, with osteoblasts lining the new woven bone and osteoid formation in multiple regions, indicates high-quality bone regeneration. The observation of osteocytes and the Haversian system in the new lamellar bone further suggests the maturation of bone tissue within the gyroid implant. These features are indicative of a healthy remodeling process, leading to the formation of strong bone tissue.[54] The observations strongly suggest that the porous architecture design of bone implants can significantly influence their cell−material interaction.

CONCLUSION

This study has demonstrated the superior performance of gyroid-based biomimetic porous structures, additively manufactured using SLM technology, for implant applications. Mesenchymal stem cells (MSCs) grown on the surface of both gyroid and dense samples exhibited similar cellular density, although the gyroid sample displayed morphological changes attributed to its inherent roughness. The gyroid structure has a 53% lower MV/TV ratio compared to the dense sample, meaning less metal volume, which directly translates to reduced mechanical properties, bringing it closer to the characteristics of natural human bone. Additionally, the gyroid structure has an 11-fold higher BV/TV ratio compared to the dense sample. The gyroids have a surface area of 248 mm^2, 185% larger than a dense sample of the same size, providing more space for cell adhesion and expansion. This resulted in significant improvement in bone growth after 6 weeks in rabbit models. The porous nature of the gyroid also facilitated improved early stage bone integration, enhancing its success rate as evidenced by histological analysis. Furthermore, the study confirmed bone ingrowth and the formation of new blood vessels alongside osteoids and Haversian canal systems, indicative of better bone remodeling.

AUTHOR INFORMATION

Corresponding Author

Geetha Manivasagam − *Centre for Biomaterials, Cellular, and Molecular Theranostics, Vellore Institute of Technology, Vellore 632014, India;* orcid.org/0000-0003-3326-3176; Email: geethamanivasagam@vit.ac.in

https://doi.org/10.1021/acsmaterialsau.4c00016
ACS Mater. Au 2024, 4, 479−488

Authors

Pearlin Amaan Khan − *Centre for Biomaterials, Cellular, and Molecular Theranostics, Vellore Institute of Technology, Vellore 632014, India*

Ansheed Raheem − *Centre for Biomaterials, Cellular, and Molecular Theranostics, Vellore Institute of Technology, Vellore 632014, India*

Cheirmadurai Kalirajan − *Centre for Biomaterials, Cellular, and Molecular Theranostics, Vellore Institute of Technology, Vellore 632014, India*

Konda Gokuldoss Prashanth − *Centre for Biomaterials, Cellular, and Molecular Theranostics, Vellore Institute of Technology, Vellore 632014, India; Tallinn University of Technology, 19086 Tallinn, Estonia;* orcid.org/0000-0001-5644-2527

Complete contact information is available at: https://pubs.acs.org/10.1021/acsmaterialsau.4c00016

Author Contributions

Conceptualization: G.M. and P.K.G.; Data curation: P.A.K. and A.R.; Formal analysis: P.A.K., A.R., C.K., P.K.G. and G.M.; Funding acquisition: P.K.G. and G.M.; Investigation: P.A.K., A.R., P.K.G. and G.M.; Methodology: P.A.K., A.R., C.K., P.K.G. and G.M.; Project administration: P.K.G. and G.M.; Resources: P.K.G. and G.M.; Software: P.A.K. and A.R.; Supervision: P.K.G. and G.M.; Validation: C.K., P.K.G. and G.M.; Visualization: P.A.K. and A.R.; Writing − original draft: P.A.K. and A.R.; Writing − review & editing: P.A.K. and A.R. CRediT: **Pearlin Amaan Khan** data curation, formal analysis, investigation, methodology, software, visualization, writing-original draft, writing-review & editing; **Ansheed Raheem** data curation, formal analysis, investigation, methodology, software, visualization, writing-original draft, writing-review & editing; **Cheirmadurai Kalirajan** formal analysis, validation, writing-review & editing; **Konda Gokuldoss Prashanth** conceptualization, formal analysis, funding acquisition, project administration, resources, supervision, validation; **Geetha Manivasagam** conceptualization, formal analysis, funding acquisition, investigation, project administration, resources, supervision, validation.

Notes

The authors declare no competing financial interest.

■ ACKNOWLEDGMENTS

The authors sincerely thank the Vellore Institute of Technology, Vellore, for providing the necessary facilities and support. We extend our thanks to the Department of Science and Technology (DST/INT/SWD/VR/P15/2019), Government of India, for their financial support of this study and for the funding of Pearlin Amaan Khan as a Senior Research Fellow within the project framework. Further, we are indebted to the Council of Scientific and Industrial Research [Grant No. 22(0803)/19/EMR-II], Government of India, for funding Ansheed Raheem as a Junior Research Fellow. Additionally, we acknowledge the Department of Biotechnology, Government of India, for their financial support to Dr. Cheirmadurai K through the DBT-RA program (DBT-RA/2021/January/N/347). We also wish to thank Aswin Gurumallesh, our MSc intern, for his invaluable support throughout the project.

■ ABBREVIATIONS

TPMS, triple periodic minimal surface; ECM, extracellular matrix; STL, stereolithography; HF/HNO_3, hydrofluoric acid/nitric acid; SEM, scanning electron microscope; hMSC, human mesenchymal stem cell; LDH, lactate dehydrogenase; FITC, fluorescein isothiocyanate; DAPI, 4′,6-diamidino-2-phenylindole; IAEC, Institutional Animal Ethical Committee; CT, computed tomography; BV, bone volume; MV, metal volume; TV, total volume; MMA, methyl methacrylate

■ REFERENCES

(1) Mastnak, T.; Maver, U.; Finšgar, M. Addressing the Needs of the Rapidly Aging Society through the Development of Multifunctional Bioactive Coatings for Orthopedic Applications. *International Journal of Molecular Sciences 2022, Vol. 23, Page 2786* **2022**, *23* (5), 2786.

(2) Orthopedic Devices Market Size, Share, & Trends Report, https://www.grandviewresearch.com/industry-analysis/orthopedic-devices-market (accessed 2024-05-03).

(3) Lozano, C. M.; Samundeeswari, S.; Araujo-Espinoza, G.; Shanmugasundaram, S. Impact of Increased Life Expectancy on Orthopaedic Trauma Implantology. *Handbook of Orthopaedic Trauma Implantology* **2023**, 951−964.

(4) Gill, T. K.; Mittinty, M. M.; March, L. M.; Steinmetz, J. D.; Culbreth, G. T.; Cross, M.; Kopec, J. A.; Woolf, A. D.; Haile, L. M.; Hagins, H.; Ong, K. L.; Kopansky-Giles, D. R.; Dreinhoefer, K. E.; Betteridge, N.; Abbasian, M.; Abbasifard, M.; Abedi, K.; Adesina, M. A.; Aithala, J. P.; Akbarzadeh-Khiavi, M.; Al Thaher, Y.; Alalwan, T. A.; Alzahrani, H.; Amiri, S.; Antony, B.; Arabloo, J.; Aravkin, A. Y.; Arumugam, A.; Aryal, K. K.; Athari, S. S.; Atreya, A.; Baghdadi, S.; Bardhan, M.; Barrero, L. H.; Bearne, L. M.; Bekele, A. B.; Bensenor, I. M.; Bhardwaj, P.; Bhatti, R.; Bijani, A.; Bordianu, T.; Bouaoud, S.; Briggs, A. M.; Cheema, H. A.; Christensen, S. W. M. P.; Chukwu, I. S.; Clarsen, B.; Dai, X.; de Luca, K.; Desye, B.; Dhimal, M.; Do, T. C.; Fagbamigbe, A. F.; Farokh Forghani, S.; Ferreira, N.; Ganesan, B.; Gebrehiwot, M.; Ghashghaee, A.; Graham, S. M.; Harlianto, N. I.; Hartvigsen, J.; Hasaballah, A. I.; Hasanian, M.; Hassen, M. B.; Hay, S. I.; Heidari, M.; Hsiao, A. K.; Ilic, I. M.; Jokar, M.; Khajuria, H.; Khan, M. J.; Khanal, P.; Khateri, S.; Kiadaliri, A.; Kim, M. S.; Kisa, A.; Kolahi, A. A.; Krishan, K.; Krishnamoorthy, V.; Landires, I.; Larijani, B.; Le, T. T. T.; Lee, Y. H.; Lim, S. S.; Lo, J.; Madani, S. P.; Malagón-Rojas, J. N.; Malik, I.; Marateb, H. R.; Mathew, A. J.; Meretoja, T. J.; Mesregah, M. K.; Mestrovic, T.; Mirahmadi, A.; Misganaw, A.; Mohaghegh, S.; Mokdad, A. H.; Momenzadeh, K.; Momtazmanesh, S.; Monasta, L.; Moni, M. A.; Moradi, Y.; Mostafavi, E.; Muhammad, J. S.; Murray, C. J. L.; Muthu, S.; Nargus, S.; Nassereldine, H.; Neupane, S.; Niazi, R. K.; Oh, I. H.; Okati-Aliabad, H.; Oulhaj, A.; Pacheco-Barrios, K.; Park, S.; Patel, J.; Pawar, S.; Pedersini, P.; Peres, M. F. P.; Petcu, I. R.; Petermann-Rocha, F. E.; Poursadeqiyan, M.; Qattea, I.; Qureshi, M. F.; Rafferty, Q.; Rahimi-Dehgolan, S.; Rahman, M.; Ramasamy, S. K.; Rashedi, V.; Redwan, E. M. M.; Ribeiro, D. C.; Roever, L.; Safary, A.; Sagoe, D.; Saheb Sharif-Askari, F.; Sahebkar, A.; Salehi, S.; Shafaat, A.; Shahabi, S.; Sharma, S.; Shashamo, B. B.; Shiri, R.; Singh, A.; Slater, H.; Smith, A. E.; Sunuwar, D. R.; Tabish, M.; Tharwat, S.; Ullah, I.; Valadan Tahbaz, S.; Vasankari, T. J.; Villafañe, J. H.; Vollset, S. E.; Wiangkham, T.; Yonemoto, N.; You, Y.; Zare, I.; Zheng, P.; Vos, T.; Brooks, P. M. Global, Regional, and National Burden of Other Musculoskeletal Disorders, 1990−2020, and Projections to 2050: A Systematic Analysis of the Global Burden of Disease Study 2021. *Lancet Rheumatol* **2023**, *5* (11), e670−e682.

(5) Rodriguez-Merchan, E. C. The Influence of Obesity on the Outcome of TKR: Can the Impact of Obesity Be Justified from the Viewpoint of the Overall Health Care System? *HSS Journal* **2014**, *10* (2), 167.

(6) Jarman, M. P.; Weaver, M. J.; Haider, A. H.; Salim, A.; Harris, M. B. The National Burden of Orthopedic Injury: Cross-Sectional

Estimates for Trauma System Planning and Optimization. *Journal of Surgical Research* **2020**, *249*, 197−204.
(7) Javaid, M.; Haleem, A. Impact of Industry 4.0 to Create Advancements in Orthopaedics. *J. Clin Orthop Trauma* **2020**, *11*, S491.
(8) Waldrop, V. H.; Laverty, D. C.; Bozic, K. J. Value-Based Healthcare: Increasing Value by Reducing Implant-Related Health Care Costs. *Clin Orthop Relat Res.* **2019**, *477* (2), 281.
(9) Pean, C. A.; Lajam, C.; Zuckerman, J.; Bosco, J. Policy and Ethical Considerations for Widespread Utilization of Generic Orthopedic Implants. *Arthroplast Today* **2019**, *5* (2), 256.
(10) Tapscott, D. C.; Wottowa, C. Orthopedic Implant Materials. *StatPearls*; StatPearls Publishing: Treasure Island (FL); 2023.
(11) Szczęsny, G.; Kopec, M.; Politis, D. J.; Kowalewski, Z. L.; Łazarski, A.; Szolc, T. A Review on Biomaterials for Orthopaedic Surgery and Traumatology: From Past to Present. *Materials* **2022**, *15* (10), 3622.
(12) Garcia-Gareta, E.; Hua, J.; Orera, A.; Kohli, N.; Knowles, J. C.; Blunn, G. W. Biomimetic Surface Functionalization of Clinically Relevant Metals Used as Orthopaedic and Dental Implants. *Biomedical Materials* **2018**, *13* (1), No. 015008.
(13) Khodaei, T.; Schmitzer, E.; Suresh, A. P.; Acharya, A. P. Immune Response Differences in Degradable and Non-Degradable Alloy Implants. *Bioact Mater.* **2023**, *24*, 153.
(14) Geetha, M.; Singh, A. K.; Asokamani, R.; Gogia, A. K. Ti Based Biomaterials, the Ultimate Choice for Orthopaedic Implants − A Review. *Prog. Mater. Sci.* **2009**, *54* (3), 397−425.
(15) Navarro, M.; Michiardi, A.; Castaño, O.; Planell, J. A. Biomaterials in Orthopaedics. *J. R Soc. Interface* **2008**, *5* (27), 1137.
(16) Rabel, K.; Kohal, R. J.; Steinberg, T.; Tomakidi, P.; Rolauffs, B.; Adolfsson, E.; Palmero, P.; Fürderer, T.; Altmann, B. Controlling Osteoblast Morphology and Proliferation via Surface Micro-Topographies of Implant Biomaterials. *Sci. Rep* **2020**, *10* (1), 12810.
(17) Yuan, L.; Ding, S.; Wen, C. Additive Manufacturing Technology for Porous Metal Implant Applications and Triple Minimal Surface Structures: A Review. *Bioact Mater.* **2019**, *4* (1), 56−70.
(18) Feller, L.; Jadwat, Y.; Khammissa, R. A. G.; Meyerov, R.; Schechter, I.; Lemmer, J. Cellular Responses Evoked by Different Surface Characteristics of Intraosseous Titanium Implants. *Biomed Res. Int.* **2015**, *2015*, 1.
(19) Saini, M.; Singh, Y.; Arora, P.; Arora, V.; Jain, K. Implant Biomaterials: A Comprehensive Review. *World Journal of Clinical Cases: WJCC* **2015**, *3* (1), 52.
(20) Raffa, M. L.; Nguyen, V. H.; Hernigou, P.; Flouzat-Lachaniette, C. H.; Haiat, G. Stress Shielding at the Bone-Implant Interface: Influence of Surface Roughness and of the Bone-Implant Contact Ratio. *J. Orthop Res.* **2021**, *39* (6), 1174−1183.
(21) Knapp, K. M.; Rowlands, A. V.; Welsman, J. R.; MacLeod, K. M. Prolonged Unilateral Disuse Osteopenia 14 Years Post External Fixator Removal: A Case History and Critical Review. *Case Rep. Med.* **2010**, *2010*, 1.
(22) Naghavi, S. A.; Lin, C.; Sun, C.; Tamaddon, M.; Basiouny, M.; Garcia-Souto, P.; Taylor, S.; Hua, J.; Li, D.; Wang, L.; Liu, C. Stress Shielding and Bone Resorption of Press-Fit Polyether−Ether−Ketone (PEEK) Hip Prosthesis: A Sawbone Model Study. *Polymers (Basel)* **2022**, *14* (21), 4600.
(23) Daubert, D. M.; Pozhitkov, A. E.; Safioti, L. M.; Kotsakis, G. A. Association of Global DNA Methylation to Titanium and Peri-Implantitis: A Case-Control Study. *JDR Clin. Trans. Res.* **2019**, *4* (3), 284−291.
(24) Hameed, P.; Liu, C.-F.; Ummethala, R.; Singh, N.; Huang, H.-H.; Manivasagam, G.; Prashanth, K. G. Biomorphic Porous Ti6Al4V Gyroid Scaffolds for Bone Implant Applications Fabricated by Selective Laser Melting. *Progress in Additive Manufacturing* **2021**, *6* (3), 455−469.
(25) Zhang, Y.; Sun, N.; Zhu, M.; Qiu, Q.; Zhao, P.; Zheng, C.; Bai, Q.; Zeng, Q.; Lu, T. The Contribution of Pore Size and Porosity of 3D Printed Porous Titanium Scaffolds to Osteogenesis. *Biomaterials Advances* **2022**, *133*, No. 112651.
(26) Große-Brauckmann, K. Gyroids of Constant Mean Curvature. *Exp Math* **1997**, *6* (1), 33−50.
(27) Dong, Z.; Zhao, X. Application of TPMS Structure in Bone Regeneration. *Engineered Regeneration* **2021**, *2*, 154−162.
(28) Wang, R.; Ni, S.; Ma, L.; Li, M. Porous Construction and Surface Modification of Titanium-Based Materials for Osteogenesis: A Review. *Front Bioeng Biotechnol* **2022**, *10*, 973297.
(29) Song, C.; Liu, L.; Deng, Z.; Lei, H.; Yuan, F.; Yang, Y.; Li, Y.; Yu, J. Research Progress on the Design and Performance of Porous Titanium Alloy Bone Implants. *Journal of Materials Research and Technology* **2023**, *23*, 2626−2641.
(30) De Jong, W. H.; Carraway, J. W.; Geertsma, R. E. In Vivo and in Vitro Testing for the Biological Safety Evaluation of Biomaterials and Medical Devices. *Biocompatibility and Performance of Medical Devices* **2020**, 123−166.
(31) Cheng, M.; Liu, W.; Zhang, J.; Zhang, S.; Guo, Z.; Liu, L.; Tian, J.; Zhang, X.; Cheng, J.; Liu, Y.; Deng, G.; Gao, G.; Sun, L. Perspective Regulatory Considerations for Animal Studies of Biomaterial Products. *Bioactive Materials* **2022**, *11*, 52.
(32) Mapara, M.; Thomas, B. S.; Bhat, K. M. Rabbit as an Animal Model for Experimental Research. *Dent Res. J. (Isfahan)* **2012**, *9* (1), 111.
(33) Wang, X.; Mabrey, J.; Agrawal, C. M. An Interspecies Comparison of Bone Fracture Properties. *Bio-Medical Materials and Engineering* **1998**, *8*, 1.
(34) Meng, X.; Ziadlou, R.; Grad, S.; Alini, M.; Wen, C.; Lai, Y.; Qin, L.; Zhao, Y.; Wang, X. Animal Models of Osteochondral Defect for Testing Biomaterials. *Biochem Res. Int.* **2020**, *2020*, 1.
(35) Wysocki, B.; Idaszek, J.; Szlazak, K.; Strzelczyk, K.; Brynk, T.; Kurzydłowski, K. J.; Święszkowski, W. Post Processing and Biological Evaluation of the Titanium Scaffolds for Bone Tissue Engineering. *Materials 2016, Vol. 9, Page 197* **2016**, *9* (3), 197.
(36) Hameed, P.; Gopal, V.; Bjorklund, S.; Ganvir, A.; Sen, D.; Markocsan, N.; Manivasagam, G. Axial Suspension Plasma Spraying: An Ultimate Technique to Tailor Ti6Al4V Surface with HAp for Orthopaedic Applications. *Colloids Surf. B Biointerfaces* **2019**, *173*, 806−815.
(37) Morgan, E. F.; Unnikrisnan, G. U.; Hussein, A. I. Bone Mechanical Properties in Healthy and Diseased States. *Annu. Rev. Biomed Eng.* **2018**, *20*, 119.
(38) Karageorgiou, V.; Kaplan, D. Porosity of 3D Biomaterial Scaffolds and Osteogenesis. *Biomaterials* **2005**, *26* (27), 5474−5491.
(39) Murphy, C. M.; Haugh, M. G.; O'Brien, F. J. The Effect of Mean Pore Size on Cell Attachment, Proliferation and Migration in Collagen−Glycosaminoglycan Scaffolds for Bone Tissue Engineering. *Biomaterials* **2010**, *31* (3), 461−466.
(40) Gokuldoss, P. K.. *Selective Laser Melting: Materials and Applications*; MDPI AG, 2020.
(41) Zareidoost, A.; Yousefpour, M.; Ghaseme, B.; Amanzadeh, A. The Relationship of Surface Roughness and Cell Response of Chemical Surface Modification of Titanium. *J. Mater. Sci. Mater. Med.* **2012**, *23* (6), 1479.
(42) Zhou, H.; Weir, M. D.; Xu, H. H. K. Effect of Cell Seeding Density on Proliferation and Osteodifferentiation of Umbilical Cord Stem Cells on Calcium Phosphate Cement-Fiber Scaffold. *Tissue Eng. Part A* **2011**, *17* (21−22), 2603.
(43) Li, G.; Wang, L.; Pan, W.; Yang, F.; Jiang, W.; Wu, X.; Kong, X.; Dai, K.; Hao, Y. In Vitro and in Vivo Study of Additive Manufactured Porous Ti6Al4V Scaffolds for Repairing Bone Defects. *Scientific Reports 2016 6:1* **2016**, *6* (1), 1−11.
(44) Majhy, B.; Priyadarshini, P.; Sen, A. K. Effect of Surface Energy and Roughness on Cell Adhesion and Growth − Facile Surface Modification for Enhanced Cell Culture. *RSC Adv.* **2021**, *11* (25), 15467−15476.
(45) Piironen, K.; Haapala, M.; Talman, V.; Järvinen, P.; Sikanen, T. Cell Adhesion and Proliferation on Common 3D Printing Materials

https://doi.org/10.1021/acsmaterialsau.4c00016
ACS Mater. Au 2024, 4, 479−488

Used in Stereolithography of Microfluidic Devices. *Lab Chip* **2020**, *20* (13), 2372−2382.
(46) Long, E. G.; Buluk, M.; Gallagher, M. B.; Schneider, J. M.; Brown, J. L. Human Mesenchymal Stem Cell Morphology, Migration, and Differentiation on Micro and Nano-Textured Titanium. *Bioact Mater.* **2019**, *4*, 249−255.
(47) *X-rays of dental implants and panoramic radiographs*. https://dental-edu.com/services/dental-implants/x-rays-of-dental-implants-panoramic-radiographs/ (accessed 2023-01-04).
(48) Yao, Y.-t.; Yang, Y.; Ye, Q.; Cao, S.-s.; Zhang, X.-p.; Zhao, K.; Jian, Y. Effects of Pore Size and Porosity on Cytocompatibility and Osteogenic Differentiation of Porous Titanium. *J. Mater. Sci. Mater. Med.* **2021**, *32* (6), 1−11.
(49) Palacio-Mancheno, P. E.; Larriera, A. I.; Doty, S. B.; Cardoso, L.; Fritton, S. P. 3D Assessment of Cortical Bone Porosity and Tissue Mineral Density Using High-Resolution Micro-CT: Effects of Resolution and Threshold Method. *J. Bone Miner Res.* **2014**, *29* (1), 142−150.
(50) Yamada, M.; Ueno, T.; Minamikawa, H.; Ikeda, T.; Nakagawa, K.; Ogawa, T. Early-Stage Osseointegration Capability of a Submicrofeatured Titanium Surface Created by Microroughening and Anodic Oxidation. *Clin Oral Implants Res.* **2013**, *24* (9), 991−1001.
(51) Koju, N.; Niraula, S.; Fotovvati, B. Additively Manufactured Porous Ti6Al4V for Bone Implants: A Review. *Metals 2022, Vol. 12, Page 687* **2022**, *12* (4), 687.
(52) Thomas, J.; Alsaleh, N. A.; Ahmadein, M.; Elfar, A. A.; Farouk, H. A.; Essa, K. Graded Cellular Structures for Enhanced Performance of Additively Manufactured Orthopaedic Implants. *International Journal of Advanced Manufacturing Technology* **2024**, *130* (3−4), 1887−1900.
(53) Feng, B.; Jinkang, Z.; Zhen, W.; Jianxi, L.; Jiang, C.; Jian, L.; Guolin, M.; Xin, D. The Effect of Pore Size on Tissue Ingrowth and Neovascularization in Porous Bioceramics of Controlled Architecture in Vivo. *Biomed Mater.* **2011**, *6* (1), 015007.
(54) *Anatomy and Ultrastructure of Bone − Histogenesis, Growth and Remodeling* - Endotext - NCBI Bookshelf. 2019, https://www.ncbi.nlm.nih.gov/books/NBK279149/ (accessed 2024-05-04).

https://doi.org/10.1021/acsmaterialsau.4c00016
ACS Mater. Au 2024, 4, 479−488